Xu et al. Earth, Planets and Space (2019) 71:93
https://doi.org/10.1186/s40623-019-1072-0

Earth, Planets and Space

FULL PAPER Open Access

Thermospheric wind variations observed by a Fabry–Perot interferometer at Tromsø, Norway, at substorm onsets

Heqiucen Xu[1*], Kazuo Shiokawa[1], Shin-ichiro Oyama[1,2,3] and Yuichi Otsuka[1]

Abstract

Energy input from the magnetosphere during substorms can strongly affect the high-latitude thermosphere. The ionospheric current caused by thermospheric wind variations may also provide a feedback to the magnetosphere. In this study, we investigate the characteristics of high-latitude thermospheric wind variations at local substorm onsets at Tromsø, Norway, as well as the possibility of such feedback mechanism. A Fabry–Perot interferometer (FPI) at Tromsø provided wind measurements estimated from the Doppler shift of red-line emission (630.0 nm) of aurora and airglow. We analyzed wind data in 2009 with a time resolution of ~ 13 min. We first carefully identified the onset times of isolated local substorms at Tromsø and extracted four wind measurements from red-line emission. All these events showed increases of eastward components at local substorm onsets. For northward components, these events showed decreases except for those at midnight. The observed wind variations at local substorm onsets were less than 49 m/s. These values are much smaller than the typical plasma convection speed in the auroral zone. We speculate that the ionospheric current caused by thermospheric wind variations at local substorm onsets does not provide strong feedback to the development of substorm expansion phase in the magnetotail. We discuss the possible causes of these wind variations in the context of plasma convection, diurnal tides, and arc-associated electric field.

Keywords: Fabry–Perot interferometer, Substorm, Thermosphere

Introduction

Substorms and collision between neutral and plasma

Substorms, which are important geomagnetic and auroral disturbances with timescales of a few hours, were first described scientifically by Akasofu (1964) and were later divided clearly into the phases of growth, expansion, and recovery (McPherron 1970). Among various models of substorm initiation, Kan (1993), Kan et al. (2011) proposed a magnetosphere–ionosphere-coupling (MIC) substorm model, which differs from the popular outside-in and inside-out substorm models (Shiokawa et al. 1997, 1998; Lui 1991a, 1991b). Kan's model focuses on the MIC process and suggests that the origin of substorm onset is located in the ionosphere, where a newly developed ionospheric current system can be caused by the ionospheric conductivity change.

Thermospheric neutral wind can also cause ionospheric current in the ionosphere. At thermospheric heights, the neutral number density is much larger than the plasma number density. At high latitudes, the neutral number density and electron number density at an altitude of 250 km are ~ 10^{15} m^{-3} and ~ 10^{11} m^{-3}, respectively (Brekke 1997). Therefore, the effect of ion-neutral collisions can strongly influence the ionospheric plasma motion. For example, the high-latitude neutral circulation can contribute to a notable Hall current system for several hours after a geomagnetic storm, which is called the "flywheel" effect (Lyons et al. 1985; Deng et al. 1991). Furthermore, the ionospheric current driven by thermospheric neutral wind may affect plasma dynamics in the magnetosphere through magnetic field line.

*Correspondence: xuheqiucen@isee.nagoya-u.ac.jp
[1] Institute for Space-Earth Environmental Research (ISEE), Nagoya University, Chikusa-ku, Nagoya 464-8601, Japan
Full list of author information is available at the end of the article

Measurements and studies of high-latitude winds using FPI

A Fabry–Perot interferometer (FPI), which measures the Doppler shift of emission lines from aurora and airglow, is a unique optical instrument. FPIs can measure the thermospheric wind from the ground-based stations and satellites (e.g., Killeen et al. 1986; Conde et al. 2001). The atoms and molecules in the thermosphere cause line emissions due to the excitation by auroral electron bombardment, solar ultraviolet (UV) absorption and photochemical reactions such as dissociative recombination and three-body reactions. Because these atoms and molecules move with the neutral wind in the thermosphere, using an FPI to monitor the Doppler shift of these line emissions can provide information about neutral wind velocities in the thermosphere. At the same time, the thermospheric temperature can also be determined by FPI (e.g., Nakamura et al. 2017). FPIs have been used to measure the thermospheric wind at ionospheric F-region altitude through red-line emission at a wavelength of 630.0 nm from atomic oxygen.

An FPI is a major diagnostic tool for thermospheric wind measurement to study high-latitude thermospheric dynamics. Through the interaction between neutral particles and plasmas, energy inputs from the magnetosphere severely affect the thermosphere and ionosphere at high latitudes. Focusing on the relationship between thermospheric wind and auroral activities, many studies have used FPI measurements (e.g., Conde and Smith 1998, Conde et al. 2001; Ishii et al. 2001, 2004). Near Tromsø, an FPI at Kiruna, Sweden, has been used in related studies as well (e.g., Rees et al. 1984; Aruliah et al. 1991, 1999). Including the use of satellite measurements, some studies focus on the thermospheric wind during specific substorm phases. Using an FPI at Tromsø, Norway, Oyama et al. (2016) studied lower thermospheric wind variations in auroral patches during the substorm recovery phase. Ritter et al. (2010) used Challenging Minisatellite Payload (CHAMP) satellite data at an altitude of 400 km in a statistical study focusing on the thermospheric response to substorm onsets. They found that the perturbation of thermospheric wind caused by substorms is weak (< 20 m/s).

Purpose of the study

Despite these previous wind measurements by FPIs at high latitudes, thermospheric wind variations at the onsets of auroral substorms are not yet well understood. In the present study, we use wind data at F-region height obtained by a ground-based FPI that can measure both the zonal and meridional wind components. We show the characteristics of wind variations before and after the local substorm onsets at F-region heights, and discuss its feedback to the development of substorm expansion phase in the magnetotail.

Instruments

Fabry–Perot interferometer

The FPI used in this study is located in Tromsø, Norway. The local time (LT) is 1 h ahead of universal time (UT) for all the events, while magnetic local time (MLT) at Tromsø is ~ 2.5 h ahead of UT. The FPI scans the sky in the five directions of north, west, south, east, and zenith as one set of vector wind measurement. The elevation angle of the sky scan is 45°. In Fig. 1, we plot the field-of-view in the five directions of the FPI sky scan over an all-sky auroral image. The FPI field-of-view in each direction is 5° in full angle as indicated by the small white circles. More detailed information about this FPI can be found in Shiokawa et al. (2012) and Oyama et al. (2010).

We selected the intervals of the FPI operation under the clear-sky conditions, which were identified using a collocated all-sky airglow imager of Optical Mesosphere Thermosphere Imagers (OMTIs, http://stdb2.isee.nagoya-u.ac.jp/omti/) (Shiokawa et al. 2009). As shown in Eq. (2) of Shiokawa et al. (2012), the eastward (northward) wind component measured by this FPI is calculated from the difference between the Doppler-shift speeds of the east (north) and west (south) directional winds. The directional wind is the wind speed which is projected on the horizontal plane from the line-of-sight wind speed. In the measurements, this method assumes a uniform horizontal wind in the field-of-view of the FPI (Shiokawa et al. 2003), which means that the zonal (meridional)

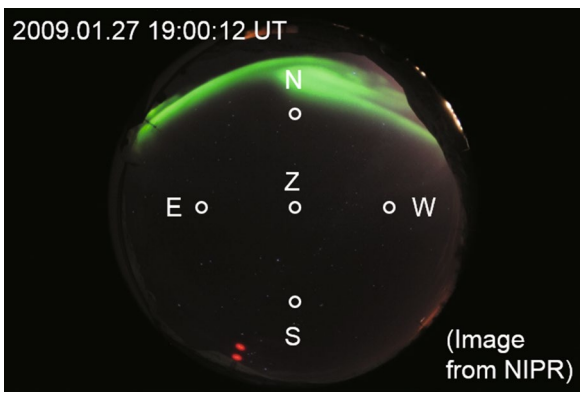

Fig. 1 Field-of-view for Fabry–Perot interferometer (FPI) measurement. The FPI scans the sky in the five directions of north, west, south, east, and zenith. The elevation angle is 45°. We plot the field-of-view of the five directions over the all-sky auroral image, as indicated by the small white circles. The field-of-view in each direction is 5°

horizontal wind is assumed to be same between the east (north) and west (south) directions of the FPI scan.

As described by Shiokawa et al. (2012), the FPI takes images of more than ten interference fringes per exposure. By measuring the Doppler shift of the peak locations of the first ten fringes from the center, the FPI determines ten individual wind speeds per exposure. Thus, there are ten values for the result of each calculated wind component. In this study, for the wind component obtained at each time t_i, we adopted the arithmetic mean v_i of the ten values as the measurement result, and used the standard deviation σ_i of the ten values to estimate the random error of the measurement due to count statistics. The estimated random error increases when the intensity of the emission becomes weaker because of a lower count rate. We abandoned those wind measurements with unreasonable values of $v_i > 500$ m/s.

Here, we should emphasize that measurements of the FPI provide the mean wind in each cycle covering the field-of-view of FPI. The area of energy dissipation induced by a discrete auroral arc is narrow. Thus, this observation mode adopting the zenith angle of 45° may not meet the ideal requirement to capture the small-scale wind acceleration induced by the discrete auroral arc. However, it is suitable for capturing wind variations on a larger scale. We also have to note that there is a possible influence from the atmospheric scattering effect. Lights that are not from the line-of-sight directions may be observed by FPI if they are scattered in the lower atmosphere (Abreu et al. 1983; Harding et al. 2017). Such situation would occur when intense aurora appears in one part of the sky and when the humidity of the lower atmosphere is high.

Other data sets

The auroral images used in this study were obtained by a collocated all-sky camera, which is provided by the National Institute of Polar Research (NIPR), Japan. This camera has a field-of-view of 180° with a fish-eye lens. The ground-based magnetometer data were provided by the International Monitor for Auroral Geomagnetic Effects (IMAGE) magnetometer network. We mainly used the magnetometer data obtained at the Tromsø and Bear Island stations. These two stations are located at almost the same geographic longitude of ~ 19° E. The Tromsø site is located at a geographic (geomagnetic) latitude of 69.66° N (66.64° N) while the Bear Island site is located at 74.50° N (71.45° N).

Event selection

Local substorm onsets and wind events

We first identified the onset times of isolated local substorms using the magnetometer data obtained at the Tromsø and Bear Island stations. A local substorm event was identified by visual inspection as an obvious decrease (> 50 nT) from the quiet-time baseline in the X-component of the magnetic field data (positive north), which was followed by recovery on a timescale of > 1 h. We chose the timing of local substorm onset as the time when the X-component starts to decrease rapidly at the Tromsø and/or Bear Island stations. In the substorm identification, we first used the data at Tromsø where the FPI measurement was made. If we identify an obvious decrease in X-component at Tromsø but the amplitude is small and/or the onset timing is ambiguous, we checked the data at Bear Island. In that case, if the Bear Island shows obvious decrease (> 50 nT) from the quiet-time baseline in the X-component, we identified it as the substorm onset. We identified isolated substorm onsets as those when there was no other substorm events with magnitude > 50 nT within 1 h before the onset times we defined. Figure 2 shows a map of Tromsø and Bear Island. Two circles indicate the typical field-of-view of all-sky camera (radius of 500 km) and FPI scanning region (radius of 250 km) at Tromsø, respectively.

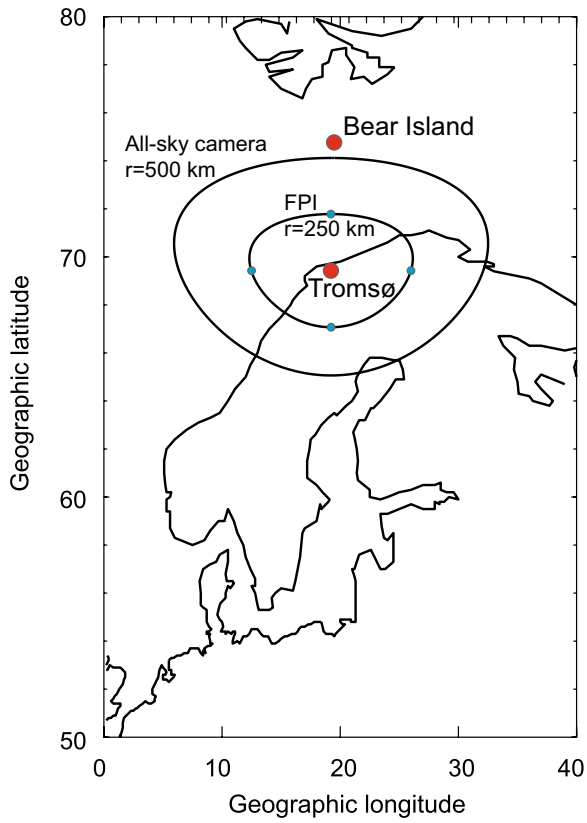

Fig. 2 A map of Tromsø and Bear Island. Two circles indicate a typical field-of-view of all-sky camera (radius of 500 km) and FPI scanning region (radius of 250 km) at Tromsø, respectively

In total, we obtained four events, which were obtained at different LTs. We only chose those events with wind measurements available both before and after the local substorm onsets. This criterion limited the number of events significantly.

Figures 3 and 4 show the X-component magnetic field variations for all the event times obtained at the Tromsø and Bear Island stations, respectively. The dashed line in each panel represents the identified local substorm onset time near Tromsø. The onset times are indicated by the text at the bottom right of each panel. The local substorm onset signatures at Tromsø can be identified in Fig. 3a, c, d, while those at Bear Island can be identified in Fig. 4b. The differing onset times at the two stations can be attributed to the differing relative locations of the peak-current latitudes.

Peak-current latitudes and global geomagnetic conditions

In addition to the X-component, we checked the latitude at which there is a peak of the westward electrojet current using the latitudinal distributions of the Z-component magnetic field variations (not shown) obtained by the IMAGE magnetometer network. We found that the peak-current latitudes were located poleward of Tromsø and equatorward of Bear Island for all the events analyzed in this paper. This is consistent with the result obtained from the all-sky auroral images, from which we found that Tromsø was located equatorward of the onset arcs for all events at the local substorm onset times. However, it is difficult to estimate the precise location of the peak current because there is no magnetic observatory between Tromsø and Bear Island.

Using the same format in Figs. 3 and 4, Fig. 5 shows the amplitude upper (AU) and amplitude lower (AL) indices for all these event times. Substorm onsets on a global scale can be identified in Fig. 5b, d after the identified local substorm onset times, whereas there were no obvious global enhancements of auroral electrojet currents for the other events. These events could be small localized substorm onsets at the longitude of Tromsø that did not expand on a global scale. Besides, there were no substorm activities elsewhere at least 1 h before the defined

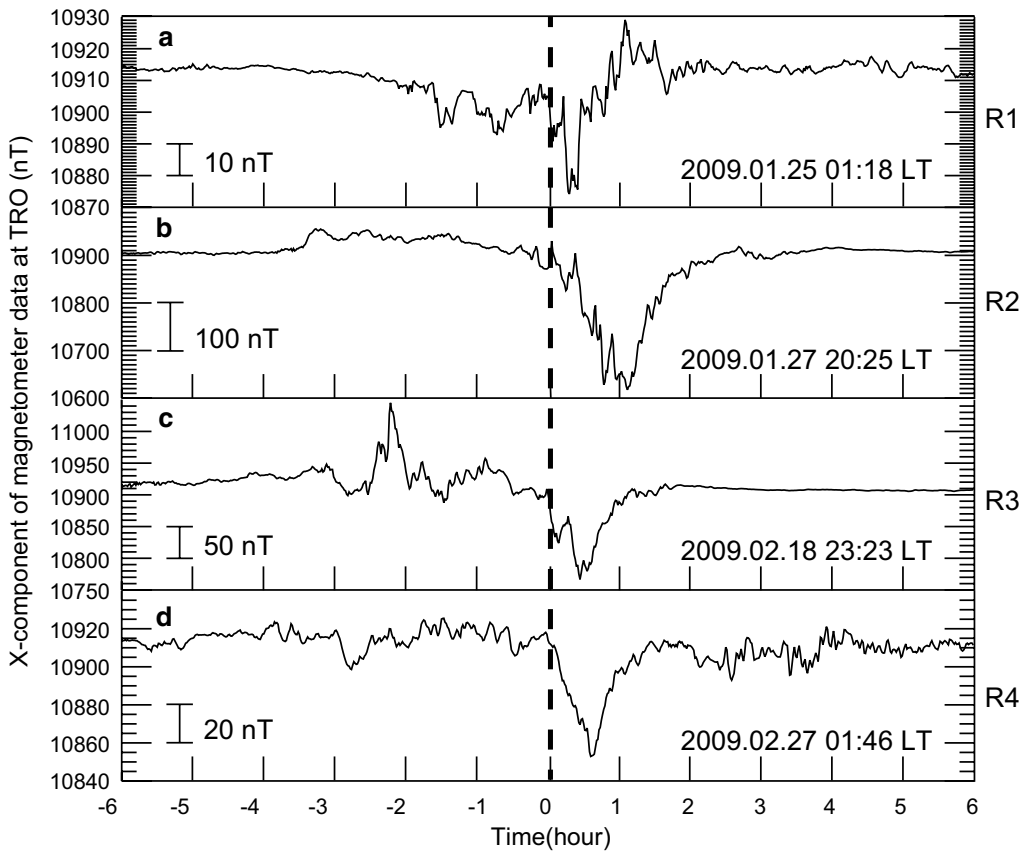

Fig. 3 X-component of 12-h ground-based magnetometer data collected at Tromsø station for all event times. Panels **a**-**d** indicate the measurements for events R1–R4, respectively. The dashed line in each panel shows the local substorm onset time near Tromsø we chose for each event. Local substorm onsets can be identified in **a**, **c** and **d**. The event time (local substorm onset time near Tromsø) shown by the text in each panel is in the format of local time (LT) at Tromsø (LT = universal time [UT] + 1 h)

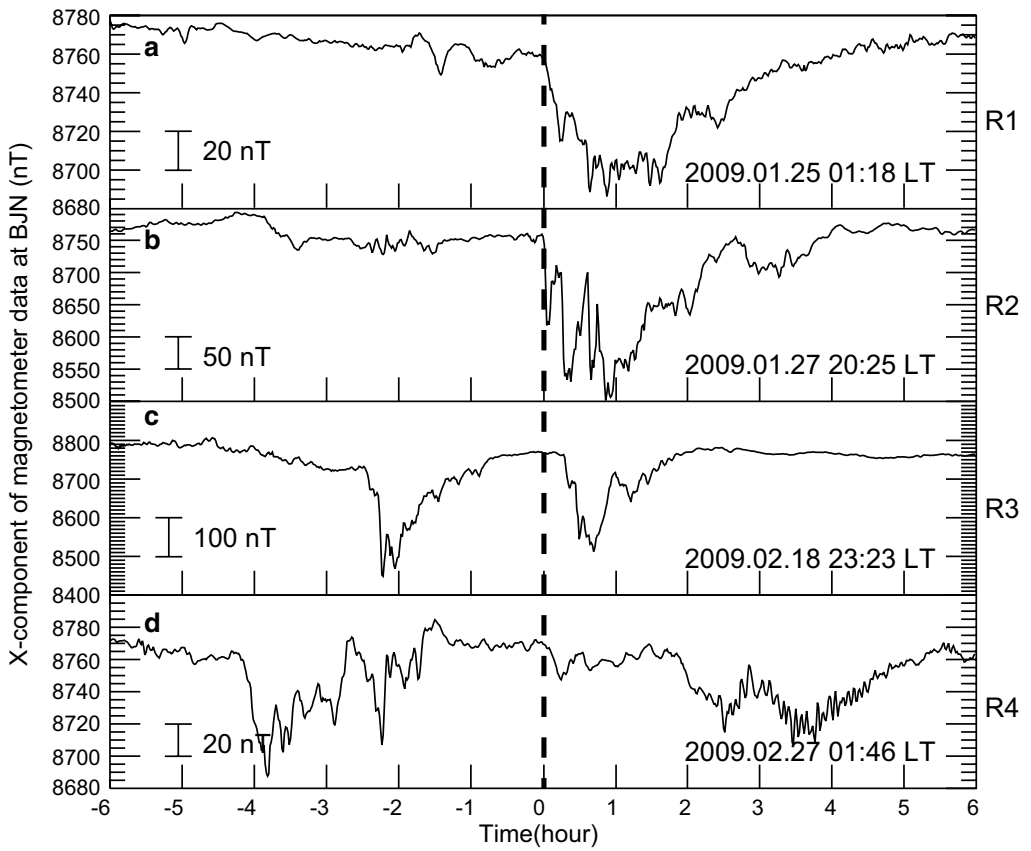

Fig. 4 X-component of 12-h ground-based magnetometer data collected at Bear Island station for all event times, using the same format in Fig. 3. Panels **a**–**d** indicate the measurements for events R1–R4, respectively. Local substorm onsets can be identified in **b**

onset times at Tromsø. The values of A_p index corresponding to the 12 h of all event times shown in Fig. 5 were between 0 and 27.

Observation results

Wind variations with cross sections of auroral images

Figures 6 and 7 show the eastward and northward components of four wind measurements plotted over the 4-h east–west cross sections (ewograms) and north–south cross sections (keograms) of the auroral images, respectively. The auroral images are in RGB color. The vertical axis in cross sections, which is basically proportional to the zenith angle of the sky, represents the number of pixel in auroral images. The ewograms and keograms are used to identify the movement of auroral activities in the zonal and meridional directions, respectively. The purple dashed lines in Figs. 6 and 7 indicate quiet-time winds at Tromsø, which were estimated from the Horizontal Wind Model (HWM) (Drob et al. 2015). HWM14 winds at altitudes of 250 km are overlaid as each reference. We chose the simultaneous A_p index as the input of HWM14, and called the model every 0.5 h. There were no all-sky camera data for ~ 10 min around 02:16 LT on 27 Feb 2009 at Tromsø. In each panel of Figs. 6 and 7, we show the local substorm onset time near Tromsø. The error bar of each wind measurement is based on the standard deviation σ_i introduced above. The two horizontal yellow lines in each panel show the east and west (north and south) points of the FPI sky scan with an elevation angle of 45° for the eastward (northward) component. The vertical red line indicates the local substorm onset time.

After the onset times of local substorms, increases of the eastward component can be observed in Fig. 6a–d (events R1–R4). The R1 and R2 events showed minimum values of the eastward component at the onset times. Before the onset times, the wind of the R2 event was westward while that of the R1 event was still eastward. This suggests that the zonal component of the R2 event was accelerated westward before the onset time, although it is unclear for the R1 event because of limited wind measurements. After the local substorm onset times, the eastward components of R1, R2 and R4 events increased for ~ 1 h.

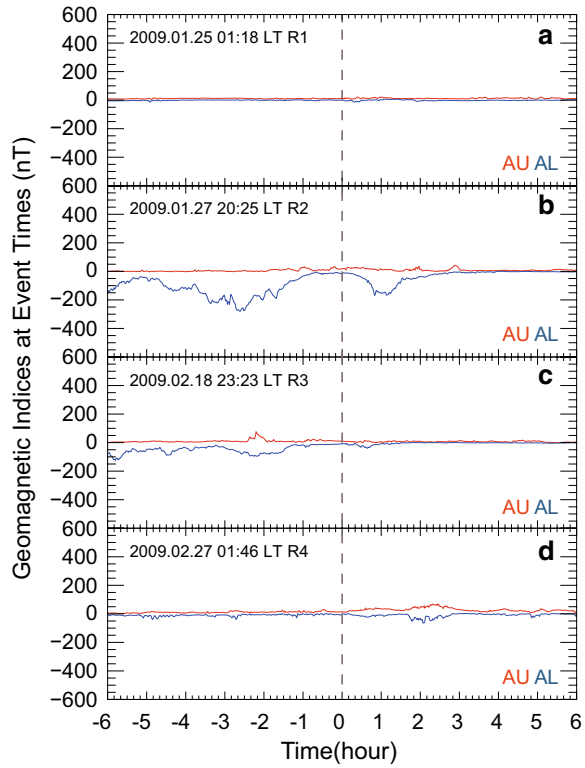

Fig. 5 AU and AL indices for all event times, using the same format in Figs. 3 and 4. Panels **a**–**d** indicate the results for events R1–R4, respectively. Global-scale substorm onsets after the local substorm onsets can be identified in **b** and **d**, while there is no obvious evidence of substorm onsets at other times

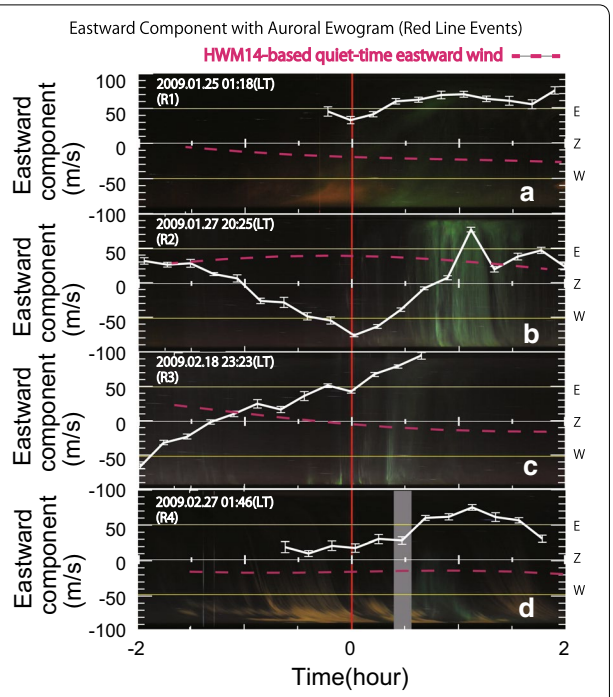

Fig. 6 Eastward component plotted over east–west cross sections of auroral images. Panels **a**–**d** indicate the measurements for events R1–R4, respectively. The horizontal yellow lines in each panel show the east and west edges of the FPI scan with an elevation angle of 45°. The vertical red lines indicate the local substorm onset times for each event, as shown by the text in the top left of each panel. For all the events, Tromsø was located at the south of the onset arc at substorm onsets. There were no all-sky camera data for ~ 10 min around 02:16 LT on 27 Feb 2009 at Tromsø

At the local substorm onset times, increase of the northward component can be identified in Fig. 7c (R3), while decreases can be observed in Fig. 7a (R1), b (R2) and d (R4). Before the local substorm onset times, the winds of all events remained southward, although it is unclear for the R1 event because of insufficient measurements. After the local substorm onset times, northward acceleration occurred in the R3 event for ~ 0.5 h. The R1 and R2 events showed decreasing northward components for > 1 h, while the R4 event decreased for ~ 0.5 h.

For the eastward components of R1 and R2 events, and northward component of R3 event, there were obvious changes in the trend of wind data at the local substorm onsets. The estimated variations at the local substorm onsets due to the tidal wind (see Fig. 9) should be a decrease of magnitude pointing to the east for these two eastward components and an increase of magnitude pointing to the south for this northward component. It seems that these abrupt changes cannot be caused by the tidal wind. The local substorm onsets probably play a more obvious role in the wind variations for these cases. Detailed discussion regarding possible explanations for these wind variations are presented in "Discussion on possible causes of wind variations" section.

Polar plots of wind variations at local substorm onsets

To evaluate the wind variations more quantitatively, we calculated the differences in average wind velocity at ± 15 min relative to the onset time and at ± 15 min relative to 30 min after the onset time. Because the standard deviation σ_i indicates the statistical error in each wind measurement, we calculated the weighted average of wind velocity $\bar{v}_{\text{onset}}$ around the substorm onset time by

$$\bar{v}_{\text{onset}} = \frac{\sum_{i=1}^{n} v_i/\sigma_i^2}{\sum_{i=1}^{n} 1/\sigma_i^2}, \tag{1}$$

where n is the number of data points during the 30 min. We also calculated the weighted average wind velocity $\bar{v}_{\text{after}}$ 30 min after the substorm onset time by applying the same equation. Then the difference $\Delta\bar{v}$ between $\bar{v}_{\text{onset}}$ and $\bar{v}_{\text{after}}$ can be written as

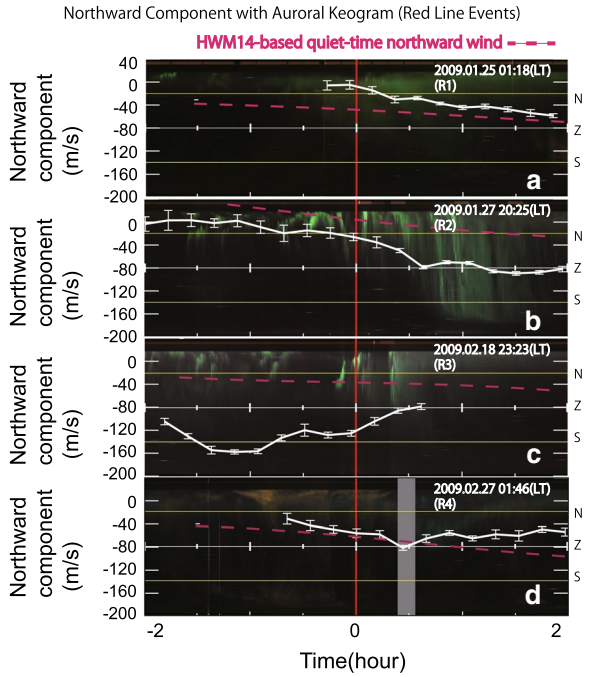

Fig. 7 Northward components plotted over north–south cross sections of auroral images, using the similar format in Fig. 6. Panels **a**–**d** indicate the measurements for events R1–R4, respectively. The horizontal yellow lines in each panel show the north and south edges of the FPI scan with an elevation angle of 45°

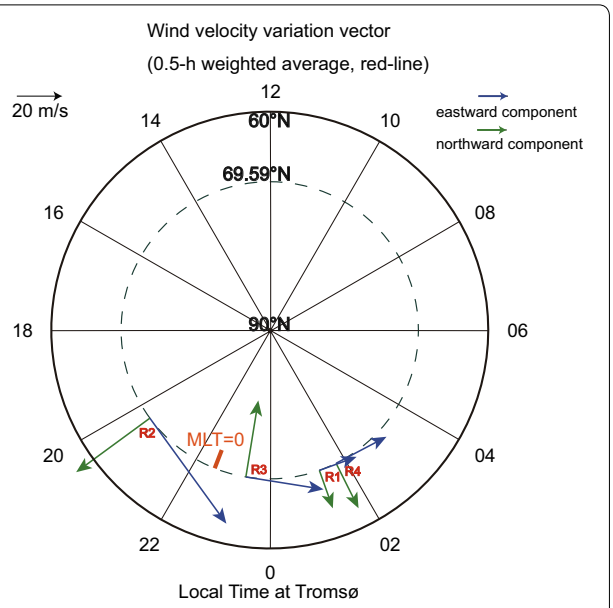

Fig. 8 Polar plot of wind variations for all four events. All eastward components showed increases, as indicated by the blue arrows. The northward components as indicated by the green arrows showed decreases except for the R3 event at midnight. The biggest wind variation was 48.9 m/s (eastward component of R2 event)

$$\Delta\bar{\nu} = \bar{\nu}_{\text{after}} - \bar{\nu}_{\text{onset}}. \quad (2)$$

This difference $\Delta\bar{\nu}$ indicates the wind variation before and after local substorm onset. For the eastward (northward) wind component, $\Delta\bar{\nu}>0$ indicates an increase, which means that the wind blows more to the east (north). On the other hand, $\Delta\bar{\nu}<0$ indicates a decrease, which means that the wind blows more to the west (south).

Figure 8 shows a polar plot of the wind variation $\Delta\bar{\nu}$ for four events. The blue (green) arrows correspond to the eastward (northward) components. The length of each arrow corresponds to the wind change calculated using Eq. (2). Note that these arrows indicate the wind difference before and after the substorm onsets. We can observe increases of the eastward wind component from the pre-midnight to post-midnight sector and decreases of the northward wind component except for the midnight sector.

The values of wind variations $\Delta\bar{\nu}$ calculated using Eq. (2) are summarized in Table 1. The observed wind variations at local substorm onsets were less than 49 m/s. These values are significant compared with the standard deviations (errors) of the FPI wind measurements. The standard deviations of the wind components used to calculate the weighted average are between 1.9 m/s and 9.7 m/s (average 4.8 m/s). The prehistory K_p index at 3–6 h before the local substorm onset times were 0^+, 2^-, 1, and 1 for R1 to R4 events, respectively. It seems that there were no strong prehistory plasma convection activities that can contribute to the observed wind variations at local substorm onsets.

Cai et al. (2019) used the same FPI (630.0 nm) at Tromsø to study thermospheric wind variations during different substorm phases. The four substorm events in their study are different from our four events and have stronger magnetic field variations. They found that the zonal wind showed a fast response to the intensification of plasma convection during the substorm expansion phase, which suggests that the ion drag contributes a lot to the acceleration of winds. In our study, we also found that the plasma convection is one important factor to affect the observed wind variations at local substorm onsets. If we assume that the observed wind variations occurred during 30 min, then the amplitudes of acceleration rates of zonal winds were 0.0097–0.0272 m/s^2 (+17.5 m/s of R1, +48.9 m/s of R2). These values are comparable with the acceleration rates of zonal winds (0.0189–0.1 m/s^2) during/near the expansion phase as summarized in Table 2 of Cai et al. (2019).

Discussion on relevance to substorm development

We showed that the neutral wind variations at local substorm onsets were less than 49 m/s for the observed four events. Ritter et al. (2010) showed the existence of an

Table 1 Observation results and discussions of four events

Red-line event (component)	Local time	Wind variation (m/s)	Diurnal tide	Plasma convection	Arc-associated electric field	Directional winds	Joule heating
R1 (East)	01:18	+17.5	N	Y	U	Y	Y
R1 (North)	01:18	−18.4	Y	N	U	N	Y
R2 (East)	20:25	+48.9	Y	N	N	U	Y
R2 (North)	20:25	−41.8	Y	Y	U	U	Y
R3 (East)	23:23	+32.3	N	Y	N	Y	Y
R3 (North)	23:23	+35.5	N	N	U	Y	Y
R4 (East)	01:46	+24.5	Y	Y	U	Y	Y
R4 (North)	01:46	−23.0	Y	N	U	Y	Y

Y wind variation is consistent with that effect (for directional winds: two winds are consistent; for Joule heating: auroral activities penetrated into the Fabry–Perot interferometer scanning region); *N* wind variation is inconsistent with that effect (for directional winds: two winds are inconsistent); *U* uncertain or not discussed

eastward wind disturbance of the order of 20 m/s in the pre-midnight and midnight sectors and a westward wind disturbance of the order of 50 m/s in the post-midnight sector associated with substorms, using measurement of the CHAMP satellite at an altitude of ~ 400 km. Thus, F-region wind variations of less than 50 m/s at local substorm onsets seem to be a common phenomenon.

The neutral wind can contribute to a notable Hall current system for several hours at high latitudes, which is called the "flywheel" effect (Lyons et al. 1985; Deng et al. 1991). At E and F regions, the electrons are hardly moved by neutral wind because of large ratio of cyclotron frequency to electron-neutral collision frequency. The neutral wind can move ions mainly in the directions of u_n (E region, Hall current) and $u_n \times B$ (F region, Pederson current), where u_n and B are horizontal neutral wind velocity and geomagnetic field, respectively (Rishbeth 1997). Therefore, the wind-induced ionospheric current is mainly carried by ions. As a feedback to the energy inputs from the magnetosphere, the wind-induced ionospheric current at local substorm onsets which is connected to the field-aligned current (FAC) can cause an inhomogeneity of magnetic tension force. This inhomogeneity may propagate along the magnetic field line and conversely influence the plasma dynamics in the near-Earth magnetosphere during the substorm expansion phase.

We can obtain the ion velocity u_i which is perpendicular to B from the simplified transport equation (Schunk and Nagy 2009):

$$u_i = \left(\frac{\nu_i \omega_{ci}}{\nu_i^2 + \omega_{ci}^2} \frac{u_n \times B}{|B|} + \frac{\nu_i^2}{\nu_i^2 + \omega_{ci}^2} u_n \right) + \left(\frac{\nu_i \omega_{ci}}{\nu_i^2 + \omega_{ci}^2} \frac{E}{|B|} + \frac{\omega_{ci}^2}{\nu_i^2 + \omega_{ci}^2} \frac{E \times B}{|B|^2} \right), \quad (3)$$

where ν_i is the ion-neutral collision frequency, ω_{ci} is the ion cyclotron frequency, E is the electric field. The left and right brackets in the right side of Eq. (3) indicate the ion velocities caused by neutral wind and electric field, respectively. Equation (3) will indicate the ion current if we multiply it by $n_i e_i$, where n_i and e_i are the ion density and electric charge of ion, respectively.

As a current generator, $u_n \times B$ acts as a similar function with E (Rishbeth 1997; Schunk and Nagy 2009). The ionospheric plasma convection is generally caused by the $E \times B$ drift. The velocity v_{drift} can be written as $E \times B/|B|^2$. The E can be written as $-v_{drift} \times B$. Mathematically, both $u_n \times B$ and $-v_{drift} \times B$ can be seen as a current generator. The comparison between u_n (or wind variations shown in this study) and v_{drift} reflects their contributions to the ionospheric current. In this study, the observed wind variations (less than 49 m/s in the F region) are much smaller than the typical plasma convection speed (hundreds of meters per second) in the auroral zone (e.g., Provan et al. 2004; Bristow and Jensen 2007), suggesting that the ionospheric current caused by the thermospheric wind variations at local substorm onsets does not provide strong feedback to the development of substorm expansion phase in the magnetotail.

Discussion on possible causes of wind variations

In this section, we discuss the possible causes of the wind variations shown in Figs. 6, 7, 8 by considering diurnal tides, plasma convection, and arc-associated electric field. We also consider spatial inhomogeneity in the FPI sky scan due to auroral Joule heating. We discuss these different mechanisms in terms of the observed direction of wind change at local substorm onsets. We summarized the consistency/inconsistency of the wind observations to these different mechanisms in Table 1. It should be noted that the tidal wind can cause wind changes with a timescale of more than several hours, while other factors associated with geomagnetic activities are more related to the shorter scale wind variation within 1 h in this study.

Diurnal tide due to pressure gradient in the F region

The two important phenomena that drive thermospheric winds at high latitudes are tides due to the day-to-night pressure gradient and plasma convection. Derived from the work of Kohl and King (1967), Fig. 9 shows a schematic drawing of the eastward and northward winds at an altitude of 300 km in the high-latitude thermosphere from 18 LT to 6 LT due to the diurnal tide. The time of zero crossing (the LTs at which the wind changes direction) for eastward component and the time of minimum value for northward component shift 2–3 h (we assumed 2 h in Fig. 9) from the midnight to the post-midnight sector. For each event, we mainly checked the direction of diurnal tide variation at the timing of local substorm onset, and compared its consistency with the observed wind variations.

In our observational results, the consistency between the directions of diurnal tide variation and wind variation can be observed in the R1 (northward component only), R2, and R4 events as indicated by "Y" in Table 1. The eastward component of the R2 event showed a continuous decrease before the onset time, which is consistent with the tendency of continuously decreasing eastward wind related to the diurnal tide. At ~ 1 h after the onset times, the eastward components of the R2 and R4 events started to decrease, which can also be explained by this diurnal tide effect.

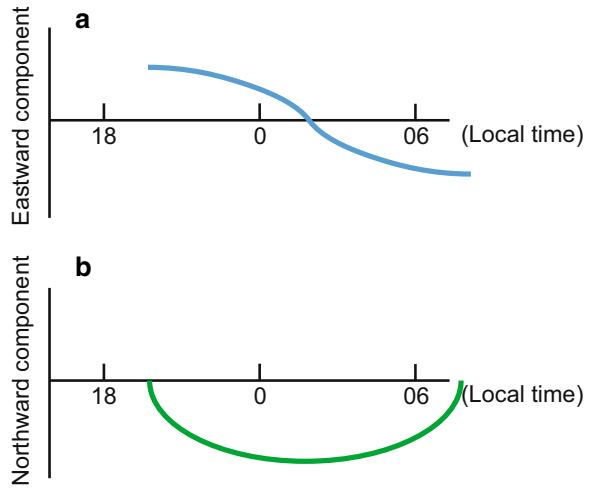

Fig. 9 Schematic of wind variations on the night-side of the Northern Hemisphere expected from the diurnal-tide model at an altitude of 300 km. The eastward component shows continuous decrease from the pre-midnight to post-midnight sector and a change of direction after the midnight. The northward component shows decrease (increase) before (after) the minimum value. The times of zero crossing and minimum value for eastward and northward components are located in the post-midnight sector around 2–3 LT

For the northward component, the R1 and R2 events showed continuous decreases during the whole measurement, which is consistent with the tendency of northward wind variation before the northward-wind minimum in the diurnal tide. The R4 event showed a U-shape variation with a minimum at ~ 30 min after the onset time, which is quite similar to the tendency of diurnal-tide-related wind variations around the northward-wind minimum as shown in Fig. 9b. As a result, five of the eight observed wind variations are consistent with the diurnal tide effect at local substorm onsets.

Plasma convection

We then investigated the effect of plasma convection at local substorm onset. We estimated the direction of plasma convection at local substorm onset using the high-latitude plasma convection model due to Weimer (1995). The convection patterns shown by Weimer (1995) were derived from the electric field measurements obtained from the Dynamics Explorer 2 (DE-2) satellite, which has a polar orbit with altitudes of 300–1000 km. Tromsø is located at the lower latitude side of the high-latitude convection pattern (see Figures 2–8 in Weimer (1995)). Basically, we expect westward and eastward plasma convection in the pre-midnight and post-midnight sectors, respectively. We assume that the convection speed increased after local substorm onsets. As we summarized in Table 1, half of the cases show consistency between the observed wind variation and the plasma convection direction at local substorm onsets. Note that three of the four eastward components show such consistency.

We should note that it may take time in the momentum transfer from plasma to neutral particles when considering the ion drag effect in the high-latitude thermospheric F region. This time constant can be 0.5–6.5 h (Baron and Wand 1983; Kosch et al. 2001). In this study, the 30-min timescale we used to calculate the wind variations is shorter than this time constant. Therefore, the wind variations due to plasma convection may not have reached a steady state in these results.

We also checked the data on actual plasma convection obtained by the Super Dual Auroral Radar Network (SuperDARN) and EISCAT radars, as well as the global plasma convection pattern from the SuperDARN radar and the data assimilation model (Ruohoniemi and Baker 1998), but did not find anything of value. There were no sufficient echoes by the SuperDARN radars at the Pykkvibaer and Hankasalmi stations for any of the event times. For the EISCAT radar, we found only a weak signal before the substorm onset at ~ 01:18 LT on January 25, 2009, for event R1. However, we could not use these data because they only provided information before the

substorm onset time. In addition, EISCAT was not operational at other event times.

Arc-associated electric field

Regarding the ion drag effect on neutral particles, besides influences of the background plasma convection discussed above, there is also an additional factor from the arc-associated ionospheric electric field. In the formation of the FAC of substorms, an intense perpendicular ionospheric electric field pointing to the auroral arc is generated locally on the equatorward (poleward) side of the auroral arc in the dusk (dawn) sector as a response to the increased upward current (e.g., Aikio et al. 1993; Burke et al. 1982; Carlson et al. 1988; Doe et al. 1995; Valladares and Carlson 1991).

At the local substorm onset times, Tromsø was located at the equatorward side of the onset arcs for all four events. Thus, we need only consider those events located at the dusk side when discussing the ion drag effect of this arc-associated electric field. For the R2 and R3 events, they were located in the dusk (pre-midnight) sector according to their solar LTs. Because the magnetic field is downward in the Northern Hemisphere, the direction of ion drag caused by the $E \times B$ drift from this arc-associated electric field is westward in the dusk sector. The observed increases in the eastward components of R2 and R3 events are inconsistent with this westward drive due to the arc-associated electric field in the pre-midnight sector, as shown by "N" in Table 1. Thus, we conclude that this mechanism of an arc-associated electric field does not work for the present four events.

Besides, this arc-associated electric field can cause the frictional heating at F-region height through ion-neutral collision (Opgenoorth et al. 1990; St.-Maurice and Hanson 1982). This would expand the neutral atmosphere and cause subsequent southward wind at Tromsø because Tromsø is always equatorward of the auroral arcs. This expansion effect is part of the discussion in the next subsection.

Spatial inhomogeneity in the FPI sky scan and auroral Joule heating

We also checked the directional winds to investigate the spatial inhomogeneity of the wind field in the field-of-view of the FPI sky scan. We compared the 4-h directional winds which are the wind components in the four directions of east, west, north and south. For the pairs of east–west and north–south directional winds, we defined them as "consistent" if anti-phase variations (same amplitudes but with opposite signs) are visually recognized. This "consistent" indicates homogeneity of the wind field in the FPI sky-scan area. In Table 1, "Y" indicates that the two directional winds are consistent while "N" indicates that they are inconsistent. An inconsistency between north and south directional winds was observed only in the R1 event, indicating that the assumption of spatial homogeneity does not hold for that case.

The last column in Table 1 corresponds to the Joule heating of auroral activities, where "Y" indicates that auroral activity penetrated into the FPI scanning region in the zonal (meridional) direction for the eastward (northward) wind component. From Figs. 6 and 7, we see the penetrations of auroral activities in all four events.

We assume that Joule heating is strong enough to change the background wind field existing near the auroral arc. Once the auroral activity penetrates into the FPI scanning region (indicated by the region between the two yellow lines in Figs. 6, 7) in the zonal (meridional) direction, the Joule heating will cause expansion of the neutral particles and affect the east (north) and west (south) directional winds in opposite directions. In such a case, inconsistent directional winds are expected to be observed.

Based on the above results and assumption, we suggest that the Joule heating effect of auroral activities influenced the wind field only for the northward wind component of the R1 event because that is the only wind component with inconsistent directional winds. It should be noted that auroral activities inside the FPI scanning region may not always affect the wind field measured by the FPI because the center location of the Joule heating may be different from the region containing the optical aurora. Besides, the Joule heating rate per mass of the neutral peaks at F-region height, although the Joule heating rate has a peak at E-region height (Deng et al. 2011). Therefore, modification of the pressure gradient due to the Joule heating process should be more obvious in the F-region thermosphere.

Summary of discussion on wind variations

As a summary, based on the directions of wind variations at local substorm onsets, we found that three of the four eastward and one of the four northward wind variations are consistent with the winds expected from plasma convection enhancement associated with substorms, and two of the four eastward and three of the four northward wind variations are consistent with the winds expected from diurnal tides. None of the wind variations can be explained by the ion drag effect from the arc-associated electric field. We attribute the inconsistency between directional winds for one northward component to the Joule heating effect from the moving auroral activity, if we assume that strong Joule heating existed near the auroral arc. These results suggest that for our observed wind variations at local substorm onsets at F-region height, they were affected mainly by plasma convection

and tidal winds, while arc-associated electric field did not significantly contribute to these processes.

We have to note that various factors can affect the wind variations simultaneously for the observed four events. A possible solution to separate individual factors might be using a 3D circulation model driven by the observations of various parameters, such as electric fields and ion densities. Liuzzo et al. (2015) studied the reliability of the Global Ionosphere–Thermosphere Model (GITM) in simulating the mesoscale wind structure at high latitudes during a substorm event. They found that modeled winds at high latitudes can be reliable only if an accurate representation of the actual drivers prevailing at the time can be identified. So we need to obtain more observation parameters to drive the model unambiguously to reproduce the high-latitude thermospheric response to the local substorm onsets.

Conclusions

Using an FPI at Tromsø in Norway, we have, for the first time, investigated the high-latitude thermospheric wind variations at local substorm onsets. We used wind data in 2009 which were measured from the Doppler shift of red-line emission (630.0 nm). In total, we obtained four red-line events, which took place at different LTs. We discussed possible causes of the wind variations by considering diurnal tides, plasma convection, and arc-associated electric field. We also considered spatial inhomogeneity in the FPI sky scan due to auroral Joule heating. Our results can be summarized as follows.

1. In this study, we assumed that the abrupt substorm energy input creates a sudden change of the thermospheric wind that may be distinguishable from the background slower effects, although the timescale of ion to neutral collision can be hours. We did observe some sudden changes of the wind direction at the time of local substorm onsets (eastward components of R1and R2 events, and northward component of R3 event).
2. The observed wind variations at local substorm onsets were less than 49 m/s at F-region height. These values are much smaller than the typical plasma convection speed in the auroral zone. We speculate that the ionospheric current caused by thermospheric wind variations at local substorm onsets does not provide strong feedback to the development of substorm expansion phase in the magnetotail.
3. At F-region height, observed events show increases of eastward winds from the pre-midnight to post-midnight sector and decreases of northward winds except for the midnight sector. We suggest that for our observed wind variations at local substorm onsets, they were affected mainly by plasma convection and tidal winds, while arc-associated electric field did not significantly contribute to these processes.

Finally, we also have to note that the conclusions of this study were based on a limited number of events. The high-latitude thermospheric responses and the role of various factors may be different for different substorm cases. More numbers of measurements about thermospheric winds and temperatures should be studied to understand the complicated thermospheric responses to the local substorm onsets.

Abbreviations

FAC: field-aligned current; FPI: Fabry–Perot interferometer; MIC: magnetosphere ionosphere coupling.

Acknowledgements

The authors acknowledge the use of SuperDARN data. SuperDARN is a collection of radars funded by national scientific funding agencies of Australia, Canada, China, France, Italy, Japan, Norway, South Africa, United Kingdom, and the United States of America. The authors acknowledge the use of the online tool hosted by the Virginia Tech SuperDARN group at their website (http://vt.superdarn.org/tiki-index.php). We are indebted to the director and staff of EISCAT for operating the facility and supplying the data. EISCAT is an international association supported by research organizations in China (CRIPR), Finland (SA), Japan (ISEE and NIPR), Norway (NFR), Sweden (VR), and the United Kingdom (STFC). We are indebted to Drs. H. Miyaoka and Y. Ogawa for operating the NIPR all-sky camera at Tromsø and supplying the data (http://polaris.nipr.ac.jp/acaurora/aurora/Tromso/). We also thank the institutes who maintain the IMAGE Magnetometer Array (http://space.fmi.fi/image/www/).

Authors' contributions

HX conducted the analysis for this study and wrote the paper. KS guided this study as the graduate-course supervisor of HX. SO and YO helped this study with the FPI measurement and use of EISCAT data. All authors have read and approved the final paper.

Funding

This work was supported by the Grant-in-Aid for Scientific Research (JP 15H05747, JP 15H05815, JP 16H02230, JP 16H06286, and JP 16K05569) from the Japan Society for the Promotion of Science. This work is partly supported by JSPS KAKENHI (16H06286). A part of work of SO was supported by the Academy of Finland project 314664. We are grateful for the support of the Leadership Development Program for Space Exploration and Research at Nagoya University.

Availability of data and materials

The wind data of FPI used in this paper are available at ISEE, Nagoya University (http://stdb2.isee.nagoya-u.ac.jp/omti/). The AU, AL, K_p and A_p indices were provided by the WDC for Geomagnetism at Kyoto University (http://wdc.kugi.kyoto-u.ac.jp). The IMF data and $F_{10.7}$ index were obtained from the GSFC/SPDF OMNIWeb interface (http://omniweb.gsfc.nasa.gov). The HWM14 model is available online (https://agupubs.onlinelibrary.wiley.com/doi/full/10.1002/2014EA000089). The IMAGE magnetometer data can be found online (http://space.fmi.fi/image/www/).
The images of all-sky camera at Tromsø are online (http://polaris.nipr.ac.jp/acaurora/aurora/Tromso/). The online tool of SuperDARN data can be found at http://vt.superdarn.org/tiki-index.php.

Ethics approval and consent to participate

Not applicable.

Consent for publication
Not applicable.

Competing interests
The authors declare that they have no competing interests.

Author details
[1] Institute for Space-Earth Environmental Research (ISEE), Nagoya University, Chikusa-ku, Nagoya 464-8601, Japan. [2] Space and Upper Atmospheric Sciences Group, National Institute of Polar Research, 10-3, Midori-cho, Tachikawa-shi, Tokyo 190-8518, Japan. [3] University of Oulu, Pentti Kaiteran katu 1, Linnanmaa, 90540 Oulu, Finland.

Received: 29 April 2019 Accepted: 21 August 2019
Published online: 30 August 2019

References

Abreu V, Schmitt GA, Hays P, Meriwether J, Tepley C, Cogger LL (1983) Atmospheric scattering effects on ground-based measurements of thermospheric winds. Planet Space Sci 31(3):303–310. https://doi.org/10.1016/0032-0633(83)90080-6

Aikio AT, Opgenoorth HJ, Persson MAL, Kaila KU (1993) Ground-based measurements of an arc-associated electric field. J Atmos Terr Phys 55:797–808. https://doi.org/10.1016/0021-9169(93)90021-P

Akasofu SI (1964) The development of the auroral substorm. Planet Space Sci 12:273–282

Aruliah AL, Rees D, Fuller-Rowell TJ (1991) The combined effect of solar and geomagnetic activity on high latitude thermospheric neutral winds. Part I. Observations. J Atmos Terr Phys 53(6–7):467–483. https://doi.org/10.1016/0021-9169(91)90075-i

Aruliah AL, Müller-Wodarg ICF, Schoendorf J (1999) Consequences of geomagnetic history on the high-latitude thermosphere and ionosphere: averages. J Geophys Res 104(A12):28073–28088. https://doi.org/10.1029/1999JA900334

Baron MJ, Wand RH (1983) F-region ion temperature enhancements resulting from Joule heating. J Geophys Res 88:4114–4118. https://doi.org/10.1029/JA088iA05p04114

Brekke A (1997) Physics of the upper polar atmosphere. Wiley, Hoboken, p 192

Bristow WA, Jensen P (2007) A superposed epoch study of SuperDARN convection observations during substorms. J Geophys Res 112:A06232. https://doi.org/10.1029/2006JA012049

Burke WJ, Gussenhoven MS, Kelley MC, Hardy DA, Rich FJ (1982) Electric and magnetic field characteristics of discrete arcs in the polar cap. J Geophys Res 87(A4):2431–2443. https://doi.org/10.1029/JA087iA04p02431

Cai L, Oyama S, Aikio A, Vanhamäki H, Virtanen I (2019) Fabry–Perot interferometer observations of thermospheric horizontal winds during magnetospheric substorms. J Geophys Res 124:3709–3728. https://doi.org/10.1029/2018JA026241

Carlson HC, Heelis RA, Weber EJ, Sharber JR (1988) Coherent mesoscale convection patterns during northward interplanetary magnetic field. J Geophys Res 93(A12):14501–14514. https://doi.org/10.1029/JA093iA12p14501

Conde M, Smith RW (1998) Spatial structure in the thermospheric horizontal wind above Poker Flat, Alaska, during solar minimum. J Geophys Res 103(A5):9449–9471. https://doi.org/10.1029/97JA03331

Conde M, Craven JD, Immel T, Hoch E, Stenbaek-Nielsen H, Hallinan T, Smith RW, Olson J, Wei Sun (2001) Assimilated observations of thermospheric winds, the aurora, and ionospheric currents over Alaska. J Geophys Res 106(A6):10493–10508. https://doi.org/10.1029/2000JA000135

Deng W, Killeen TL, Burns AG, Roble RG (1991) The flywheel effect: ionospheric currents after a geomagnetic storm. Geophys Res Lett 18:1845–1848. https://doi.org/10.1029/91GL02081

Deng Y, Fuller-Rowell TJ, Akmaev RA, Ridley AJ (2011) Impact of the altitudinal Joule heating distribution on the thermosphere. J Geophys Res 116:A05313. https://doi.org/10.1029/2010JA016019

Doe RA, Vickrey JF, Mendillo M (1995) Electrodynamic model for the formation of auroral ionospheric cavities. J Geophys Res 100(A6):9683–9696. https://doi.org/10.1029/95JA00001

Drob DP, Emmert JT, Meriwether JW, Makela JJ, Doornbos E, Conde M, Hernandez G, Noto J, Zawdie KA, McDonald SE et al (2015) An update to the Horizontal Wind Model (HWM): the quiet time thermosphere. Earth Space Sci 2:301–319. https://doi.org/10.1002/2014EA000089

Harding BJ, Makela JJ, Qin J, Fisher DJ, Martinis CR, Noto J, Wrasse CM (2017) Atmospheric scattering effects on ground-based measurements of thermospheric vertical wind, horizontal wind, and temperature. J Geophys Res 122:7654–7669. https://doi.org/10.1002/2017JA023942

Ishii M, Conde M, Smith RW, Krynicki M, Sagawa E, Watari S (2001) Vertical wind observations with two Fabry–Perot interferometers at Poker Flat, Alaska. J Geophys Res 106(A6):10537–10551

Ishii M, Kubota M, Conde M, Smith RW, Krynicki M (2004) Vertical wind distribution in the polar thermosphere during Horizontal E Region Experiment (HEX) campaign. J Geophys Res 109:A12311. https://doi.org/10.1029/2004JA010657

Kan JR (1993) A global magnetosphere-ionosphere coupling model of substorms. J Geophys Res 98(A10):17263–17275

Kan JR, Li H, Wang C, Frey HU, Kubyshkina MV, Runov A, Xiao CJ, Lyu LH, Sun W (2011) Brightening of onset arc precedes the dipolarization onset: THEMIS observations of two events on 1 March 2008. Ann Geophys 29:2045–2059. https://doi.org/10.5194/angeo-29-2045-2011

Killeen TL et al (1986) Mean neutral circulation in the winter polar F region. J Geophys Res 91(A2):1633–1649. https://doi.org/10.1029/JA091iA02p01633

Kohl H, King JW (1967) Atmospheric winds between 100 and 700 km and their effects on the ionosphere. J Atmos Terr Phys 29:1045–1062. https://doi.org/10.1016/0021-9169(67)90139-0

Kosch MJ, Cierpka K, Rietveld MT, Hagfors T, Schlegel K (2001) High-latitude ground-based observations of the thermospheric ion-drag time constant. Geophys Res Lett 28:1395–1398. https://doi.org/10.1029/2000GL012380

Liuzzo LR, Ridley AJ, Perlongo NJ, Mitchell EJ, Conde M, Hampton DL, Bristow WA, Nicolls MJ (2015) High-latitude ionospheric drivers and their effects on wind patterns in the thermosphere. J Geophys Res 120:715–735. https://doi.org/10.1002/2014JA020553

Lui ATY (1991a) A synthesis of magnetospheric substorm models. J Geophys Res 96:1849–1856

Lui ATY (1991b) Extended consideration of a synthesis model for magnetospheric substorms. In: Kan JR et al (eds) magnetospheric substorms, vol 64. AGU, Washington, D.C, pp 3–60

Lyons LR, Killeen TL, Walterscheid RL (1985) The neutral "flywheel" as a source of quiet-time polar cap currents. Geophys Res Lett 12:101–104. https://doi.org/10.1029/GL012i002p00101

McPherron RL (1970) Growth phase of magnetospheric substorms. J Geophys Res 75:5592–5599. https://doi.org/10.1029/JA075i028p05592

Nakamura Y, Shiokawa K, Otsuka Y, Oyama S, Nozawa S, Komolmis T, Komonjida S, Neudegg D, Yuile C, Meriwether J, Shinagawa H, Jin H (2017) Measurement of thermospheric temperatures using OMTI Fabry–Perot interferometers with 70-mm etalon. Earth Planets Space. 69:57. https://doi.org/10.1186/s40623-017-0643-1

Opgenoorth HJ, Hägström I, Williams PJS, Jones GOL (1990) Regions of strongly enhanced perpendicular electric fields adjacent to auroral arcs. J Atmos Terr Phys 52:449–458. https://doi.org/10.1016/0021-9169(90)90044-N

Oyama S, Shiokawa K, Kurihara J, Tsuda TT, Nozawa S, Ogawa Y, Otsuka Y, Watkins BJ (2010) Lower-thermospheric wind fluctuations measured with an FPI during pulsating aurora at Tromsø, Norway. Ann Geophys 28:1847–1857. https://doi.org/10.5194/angeo-28-1847-2010

Oyama S, Shiokawa K, Miyoshi Y, Hosokawa K, Watkins BJ, Kurihara J, Tsuda TT, Fallen CT (2016) Lower thermospheric wind variations in auroral patches during the substorm recovery phase. J Geophys Res 121:3564–3577. https://doi.org/10.1002/2015JA022129

Provan G, Lester M, Mende SB, Milan SE (2004) Statistical study of high-latitude plasma flow during magnetospheric substorms. Ann Geophys 22:3607–3624

Rees D, Lloyd N, Charleton PJ, Carlson M (1984) Comparison of plasma flow and thermospheric circulation over northern Scandinavia using EISCAT and a Fabry–Perot interferometer. J Atmos Terr Phys 46:545–564. https://doi.org/10.1016/0021-9169(84)90073-4

Rishbeth H (1997) The ionospheric E-layer and F-layer dynamos-a tutorial review. J Atmos Terr Phys 59:1873–1880. https://doi.org/10.1016/S1364-6826(97)00005-9

Ritter P, Lühr H, Doornbos E (2010) Substorm-related thermospheric density and wind disturbances derived from CHAMP observations. Ann Geophys 28:1207–1220. https://doi.org/10.5194/angeo-28-1207-2010

Ruohoniemi JM, Baker KB (1998) Large-scale imaging of high-latitude convection with Super Dual Auroral Radar Network HF radar observations. J Geophys Res 103(A9):20797–20811. https://doi.org/10.1029/98JA01288

Schunk R, Nagy A (2009) Ionospheres:physics, plasma physics, and chemistry, 2nd edn. Cambridge University Press, Cambridge, pp 139–140

Shiokawa K, Baumjohann W, Haerendel G (1997) Braking of high-speed flows in the near-Earth tail. Geophys Res Lett 10:1179–1182

Shiokawa K, Baumjohann W, Haerendel G, Paschmann G, Fennell JF, Friis-Christensen E, Lühr H, Reeves GD, Russell CT, Sutcliffe PR, Takahashi K (1998) High-speed ion flow, substorm current wedge, and multiple Pi 2 pulsations. J Geophys Res 103:4491–4507

Shiokawa K, Kadota T, Otsuka Y, Ogawa T, Nakamura T, Fukao S (2003) A two-channel Fabry–Perot interferometer with thermoelectric-cooled CCD detectors for neutral wind measurement in the upper atmosphere. Earth Planets Space 55(5):271–275

Shiokawa K, Hosokawa K, Sakaguchi K, Ieda A, Otsuka Y, Ogawa T, Connors M (2009) The optical mesosphere thermosphere imagers (OMTIs) for network measurements of aurora and airglow, future perspectives of space plasma and particle instrumentation and international collaborations. In: AIP Conference proceedings, edited by Hirahara M, Miyoshi Y, Terada N, Shinohara I, Mukai T. AIP Conference proceedings, pp 212–215. https://doi.org/10.1063/1.3169292

Shiokawa K, Otsuka Y, Oyama S, Nozawa S, Satoh M, Katoh Y, Hamaguchi Y, Yamamoto Y, Meriwether J (2012) Development of lowcost sky-scanning Fabry–Perot interferometers for airglow and auroral studies. Earth Planets Space 64(11):1033–1046. https://doi.org/10.5047/eps.2012.05.004

St.-Maurice JP, Hanson WB (1982) Ion frictional heating at high latitudes and its possible use for an in situ determination of neutral thermospheric winds and temperature. J Geophys Res 87(A9):7580–7602

Valladares CE, Carlson HC Jr (1991) The electrodynamic, thermal, and energetic character of intense Sun-aligned arcs in the polar cap. J Geophys Res 96(A2):1379–1400. https://doi.org/10.1029/90JA01765

Weimer DR (1995) Models of high-latitude electric potentials derived with a least error fit of spherical harmonic coefficients. J Geophys Res 100:19595–19607

Publisher's Note